Modeling of load reversals at very small strains in anisotropic soil with multilaminate constitutive models

Schädlich, Bert
Computational Geotechnics Group, Institute for Soil Mechanics and Foundation Engineering, Graz University of Technology, Graz, Austria, bert.schaedlich@tugraz.at

Schweiger, H. F.
Computational Geotechnics Group, Institute for Soil Mechanics and Foundation Engineering, Graz University of Technology, Graz, Austria

Keywords: anisotropy, small strain stiffness, multilaminate soil model

ABSTRACT: Although noticed very early in laboratory soil testing, anisotropic soil behavior at the small strain level is rarely taken into account in the analysis of geotechnical boundary value problems. While some recent studies (Schädlich and Schweiger 2010, Schweiger and Schädlich 2011) show that the impact of anisotropy in small strain stiffness is rather limited in typical geotechnical boundary value problems involving intermediate to large strains, the influence of anisotropy increases at smaller strains. This study focuses on modeling anisotropic small strain stiffness in multilaminate soil models and its dependency on strain history at load reversals. Evolution of strain history and load reversal is memorized in strain contours on multilaminate plane level, which enables the enforcement of all four Masing rules (Pyke 1979). Model predictions are compared with experimental data on cross-anisotropic Ham River sand at small load cycles.

1. INTRODUCTION

The phenomenon of high initial elastic stiffness of soils at very small strains ($< 10^{-6}$) and its degradation with accumulation of strain has been investigated since the early 1970ies. Taking that effect into account has become engineering practice within the last decade, in particular when realistic ground settlement predictions are required.

Still, in most practical cases soil is assumed to behave isotropically at very small strains, although laboratory tests on natural soils indicate strongly cross-anisotropic behavior (Fioravente 2000, Kuwano and Jardine 2002, Gasparre 2005).

In the following study an approach to model inherently cross-anisotropic elastic material, degradation of small strain stiffness and monitoring of strain history within the multilaminate framework is presented. Model results are compared with experimental data on anisotropic Ham River sand.

2. BASIC MULTILAMINATE MODEL

Multilaminate constitutive models are based on the concept that the material behavior can be formulated on a distinct number of local planes with varying orientation. Each plane represents a sector of a virtual sphere of unit radius around the stress point and is assigned a weight factor according to the proportion of its sector with regard to the volume of the unit sphere. The stress – strain state can vary from plane to plane, resulting in loading induced anisotropy within an intrinsically isotropic material. The global response of the material to a prescribed load is obtained by summation of the contributions of all planes.

Within the multilaminate concept the local stresses are assumed to be a projection of the global stress state (static constraint). Conceptually similar models based on the kinematic constraint (local strain increments are a projection of the global strain increment) are the so-called microplane models (Bažant and Prat 1988).

The multilaminate constitutive model presented in this study is an extension of existing elastoplastic models of this type (Schweiger et al. 2007). In the following a compacted description of the stress point algorithm for isotropic material is given.

The macroscopic trial stress $\sigma_{gl,trial}$ is calculated from the global compliance matrix C_{gl} and the global strain increment $d\varepsilon_{gl}$, which is assumed to be elastic in the first iteration. C_{gl} is derived as the weighted and projected sum of the local compliances C_{loc}.

$$\boldsymbol{\sigma}_{gl,trial} = \mathbf{C}_{gl} \cdot d\boldsymbol{\varepsilon}_{gl} + \boldsymbol{\sigma}_{gl,old} \tag{1}$$

$$\mathbf{C}_{gl} = 3 \cdot \sum_i \left(\mathbf{T}_i \cdot \mathbf{C}_{i,loc} \cdot \mathbf{T}_i^T \cdot w_i \right) \tag{2}$$

$$\mathbf{C}_{loc} = \begin{pmatrix} Cnn & 0 & 0 \\ 0 & Ctt & 0 \\ 0 & 0 & Ctt \end{pmatrix} \tag{3}$$

$$Cnn = \frac{1-2\nu}{E}; \quad Ctt = \frac{1+3\nu}{E} \tag{4}$$

In the case of isotropic linear elastic material, C_{loc} is equal for all planes. For non-linear elasticity (small strain stiffness), C_{loc} depends on the strain history of each plane and therefore differs from plane to plane, resulting in anisotropic global behavior.

The factor of 3 in front of the summation can be derived from the principle of virtual work (Bažant and Prat 1988) by comparing the sum of local work contributions and the macroscopic work. The weight factors w_i depend on the chosen integration rule. In this study an integration rule based on 2 × 33 planes (Bažant and Oh 1985) is used, which proved to balance well between accuracy and computational cost.

The transformation matrix T_i contains the derivatives of the local stress components with respect to the global stress state. Using a fixed set of local coordinates represented by the unit vector $n_i^T = (n_{i,1}, n_{i,2}, n_{i,3})$ normal to the plane i and two unit tangential vectors within the plane, $s_i^T = (s_{i,1}, s_{i,2}, s_{i,3})$ and $t_i^T = (t_{i,1}, t_{i,2}, t_{i,3})$, these derivates take on constant scalar values.

$$\mathbf{T}_i = \frac{\partial \boldsymbol{\sigma}_{i,loc}}{\partial \boldsymbol{\sigma}_{gl}} = \begin{pmatrix} n_{i,1}^2 & n_{i,1} \cdot s_{i,1} & n_{i,1} \cdot t_{i,1} \\ n_{i,2}^2 & n_{i,2} \cdot s_{i,2} & n_{i,2} \cdot t_{i,2} \\ n_{i,3}^2 & n_{i,3} \cdot s_{i,3} & n_{i,3} \cdot t_{i,3} \\ 2n_{i,1} \cdot n_{i,2} & n_{i,1} \cdot s_{i,2} + n_{i,2} \cdot s_{i,1} & n_{i,1} \cdot t_{i,2} + n_{i,2} \cdot t_{i,1} \\ 2n_{i,2} \cdot n_{i,3} & n_{i,3} \cdot s_{i,2} + n_{i,2} \cdot s_{i,3} & n_{i,3} \cdot t_{i,2} + n_{i,2} \cdot t_{i,3} \\ n_{i,1} \cdot n_{i,3} & n_{i,3} \cdot s_{i,1} + n_{i,1} \cdot s_{i,3} & n_{i,3} \cdot t_{i,1} + n_{i,1} \cdot t_{i,3} \end{pmatrix} \tag{5}$$

By projecting the global trial stress vector $\sigma_{gl,trial}$ with the transformation matrix T_i on plane i, the local trial stress vectors $\sigma_{i,loc}$ are obtained for all planes:

$$\boldsymbol{\sigma}_{i,loc} = \begin{pmatrix} \sigma_{n,i} \\ \tau_{s,i} \\ \tau_{t,i} \end{pmatrix} = \left(\mathbf{T}_i \right)^T \cdot \boldsymbol{\sigma}_{gl,trial} \tag{6}$$

Plastic strains are calculated locally based on strain hardening elastoplasticity. For details on the yield functions f, the related plastic potential functions g and the strain hardening rules see Schweiger et al. (2007).

$$d\boldsymbol{\varepsilon}_{i,loc}^{pl} = \lambda_{i,v} \cdot \frac{\partial g_{i,v}}{\partial \boldsymbol{\sigma}_{i,loc}} + \lambda_{i,d} \cdot \frac{\partial g_{i,d}}{\partial \boldsymbol{\sigma}_{i,loc}} + \lambda_{i,t} \cdot \frac{\partial g_{i,t}}{\partial \boldsymbol{\sigma}_{i,loc}} \tag{7}$$

$$\lambda_i = \frac{f^{trial}}{\frac{\partial f_i}{\partial \boldsymbol{\sigma}_{i,loc}} \cdot \mathbf{C}_{i,loc}^{-1} \cdot \frac{\partial g_i}{\partial \boldsymbol{\sigma}_{i,loc}} - \frac{\partial f_i}{\partial \boldsymbol{\varepsilon}_{i,loc}^{pl}} \cdot \frac{\partial g_i}{\partial \boldsymbol{\sigma}_{i,loc}}} \tag{8}$$

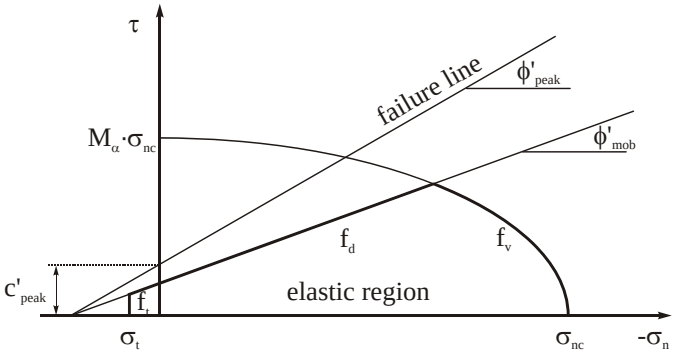

Figure 1. Volumetric, deviatoric and tension yield surface

Back-transformation and summation of all local plastic strains delivers the global plastic strain increment:

$$d\boldsymbol{\varepsilon}_{gl}^{pl} = 3 \cdot \sum_i \mathbf{T}_i \cdot d\boldsymbol{\varepsilon}_{i,loc}^{pl} \cdot w_i \tag{9}$$

The new global trial stress is then calculated with the difference of the total strain increment and the plastic strain increment.

$$\boldsymbol{\sigma}_{gl,trial} = \mathbf{C}_{gl} \cdot \left(d\boldsymbol{\varepsilon}_{gl} - d\boldsymbol{\varepsilon}_{gl}^{pl} \right) + \boldsymbol{\sigma}_{gl,old} \tag{10}$$

This iterative procedure is repeated until the plastic strain increment of the current iteration is less than 1% of the total plastic strains calculated in that step.

3. ANISOTROPIC SMALL STRAIN STIFFNESS

3.1 Concept

The elastoplastic stress point algorithm discussed above is based on the assumption, that the local stress state can be represented by 3 local stress components parallel to the axes n, t and s. As for the plastic strain calculation only the plane normal stress σ_n and the resultant shear stress τ are used, this is also known as the normal-tangential split (N-T-split). The local compliance matrix has a diagonal structure, which means normal elastic strains are only caused by normal stresses and shear strains are only caused by tangential stresses.

However, for anisotropic elastic material, that approach is not sufficient. Isotropic compression of an cross anisotropic material results in shear strains on all planes which are not parallel to the global axes, even though there is no shear stress on these planes. Hence,

the local compliance matrix of such a material obviously needs to contain off-diagonal terms.

Local compliance matrices can be obtained directly by the spectral decomposition of the global anisotropic compliance matrix. The adaptation of the method to the multilaminate framework is described in Schädlich and Schweiger (2010), therefore only the relevant results are presented here.

The local compliance matrices $C_{i,loc}$ are obtained from the sum of the product of eigenvalues λ_m and idempotent decomposing matrices E_m of the global compliance matrix, which is then projected into the plane coordinate system (eq. 11). The global compliance matrix of a cross-anisotropic material possesses four eigenvalues and four corresponding idempotent matrices, which are given in the Appendix.

$$\mathbf{C}_{i,loc} = \mathbf{T}_i^T \cdot \sum_m \boldsymbol{\lambda}_m \cdot \mathbf{E}_m \cdot \left(\mathbf{T}_i^T\right)^{-1} \tag{11}$$

As the idempotent matrices are 6x6 square matrices, also the transformation matrices need to be of that order. As a consequence, six local stress and strain components are required. These can be defined as

$$\boldsymbol{\sigma}_{i,loc} = \begin{pmatrix} \sigma_{i,n,vol} \\ \sigma_{i,n,dev} \\ \tau_{i,s1} \\ \tau_{i,s2} \\ \tau_{i,t1} \\ \tau_{i,t2} \end{pmatrix}; \quad \boldsymbol{\varepsilon}_{i,loc} = \begin{pmatrix} \varepsilon_{i,n,vol} \\ \varepsilon_{i,n,dev} \\ \gamma_{i,s1} \\ \gamma_{i,s2} \\ \gamma_{i,t1} \\ \gamma_{i,t2} \end{pmatrix} \tag{12}$$

with $\sigma_{i,n,vol}$ … volumetric normal stress, $\sigma_{i,n,dev}$ … deviatoric normal stress, $\tau_{i,s1}$ and $\tau_{i,t1}$ … tangential stresses in direction of s and t resulting from global axial stresses, $\tau_{i,s2}$ and $\tau_{i,t2}$ … tangential stresses in direction of s and t resulting from global shear stresses. As a consequence also the transformation matrices T_i need to be modified (Schädlich and Schweiger 2010). For the calculation of plastic strains local elastic strain components are summed up again to obtain ε_n, γ_s and γ_t.

3.2 Stiffness degradation

The degradation of local small strain stiffness depends on the magnitude of the local shear strain γ on that plane and is described by a logarithmic function (eq. 14). Initially all planes start with the same global anisotropic stiffness, which is projected into the plane coordinate system. The parameters γ_1 and γ_2 define the onset of degradation and the transition to large strain (isotropic) behavior. As the planes are reaching the transition to large strains at different stages of the global stress-strain curve, the material globally still behaves anisotropic, even though some planes may already have reached the isotropic stage.

$$E_h = E_{h0} - (E_{h0} - E_{ur}) \cdot \mathrm{deg} \tag{13}$$

$$\begin{aligned} &\gamma \le \gamma_1 : \mathrm{deg} = 0 \\ &\gamma_1 \le \gamma \le \gamma_2 : \mathrm{deg} = \frac{\log(\gamma) - \log(\gamma_1)}{\log(\gamma_2) - \log(\gamma_1)} \\ &\gamma \ge \gamma_2 : \mathrm{deg} = 1 \end{aligned} \tag{14}$$

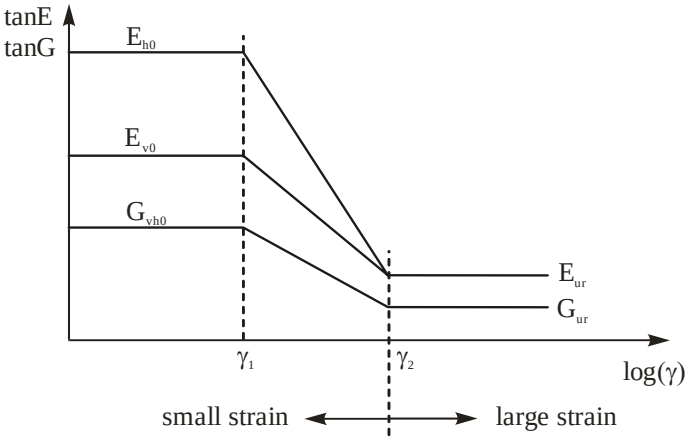

Figure 2. Degradation of anisotropic small strain stiffness (Schaedlich et al. 2010)

3.3 Stress level dependency of stiffness

In the present study two approaches for modeling the dependency of local stiffness moduli on effective stress level are investigated. In approach 1 stiffness moduli depend on the mean effective stress p', while in approach 2 dependency on the effective normal stress of the current integration plane is assumed. In both cases Poisson's ratios ν_{hh} and ν_{hv} do not change with stress level. The reference stress p_{ref} is taken as 100kPa.

Approach 1:

$$E_h = E_{h,ref} \cdot \left(\frac{p'}{p_{ref}}\right)^m; \quad E_v = E_{v,ref} \cdot \left(\frac{p'}{p_{ref}}\right)^m$$

$$G_{vh} = G_{vh,ref} \cdot \left(\frac{p'}{p_{ref}}\right)^m \tag{15}$$

Approach 2:

$$E_h = E_{h,ref} \cdot \left(\frac{\sigma_n}{p_{ref}}\right)^m; \quad E_v = E_{v,ref} \cdot \left(\frac{\sigma_n}{p_{ref}}\right)^m$$

$$G_{vh} = G_{vh,ref} \cdot \left(\frac{\sigma_n}{p_{ref}}\right)^m \tag{16}$$

3.4 Plastic strains and transition to large strain behavior

When a small strain stiffness approach as the one presented above is coupled with an elastoplastic model, calculation of plastic strains within the small strain

range needs to be modified in order to obtain the desired high initial stiffness. In the present model the volumetric and deviatoric yield surfaces are shifted such that the distance between the elastic trial stress and the current yield surface is reduced. As long as the local shear strain γ is smaller than γ_1, no plastic strains are calculated at all (full shift of yield surfaces). If $\gamma > \gamma_1$, partial shift of the yield surface is performed according to the value of (1-deg). For $\gamma > \gamma_2$ the yield surfaces are not modified any more. As a result degradation of small strain stiffness takes place faster in primary loading than in unloading/reloading (Figure 3). In both cases the same initial stiffness is obtained.

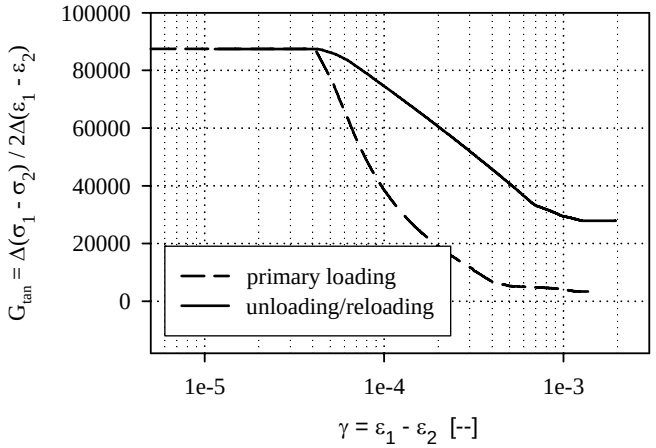

Figure 3. Degradation of isotropic small strain stiffness in primary loading and unloading / reloading

Transition of elastic parameters from small strains to large strains is accounted for automatically, as the anisotropic small strain stiffness moduli and Poisson's ratios approach large strain isotropic values E_{ur} and ν_{ur} with increasing local shear strain γ (Figure 2).

4. STRAIN HISTORY AND LOAD REVERSALS

The tangential shear stiffness in non-monotonic loading does not only depend on the magnitude of the accumulated shear strain but also on the load history. It is commonly acknowledged that reversing the direction of loading results in at least partial recovery of small strain stiffness. However, in numerical modeling different approaches have been followed regarding the driving forces of load history. While kinematic hardening models monitor load history in stress space, defining load history in strain space has been applied in other models (Simpson 1992, Benz et al. 2009). While each approach has its merits, monitoring load history in terms of strains appears to be more consistent with stiffness degradation, which is also driven by strains.

In this study strain history is memorized on each plane separately in circular contours which represent levels of equal shear strain. Each contour is defined by its centre coordinates and radius in the γ_s-γ_t- strain diagram. The degradation shear strain γ_{deg} is defined as the distance of the current shear strain state (γ_s, γ_t) to the centre of the currently active strain contour:

$$\gamma_{deg} = \sqrt{\left(\gamma_s - \gamma_{s,centre}\right)^2 + \left(\gamma_t - \gamma_{t,centre}\right)^2} \tag{17}$$

By default the innermost strain contour is active. If the current load steps reduces γ_{deg}, calculated from the innermost shear strain contour, load reversal is indicated and a new strain contour is created. If on the other hand the current load step increases γ_{deg}, calculated from one of the outer contours, an intersection with a previously followed strain path is detected, and the previous strain path is continued further on. In that case the inner strain contours are erased from the strain history of the stress point. The different cases are shown schematically in Figure 4.

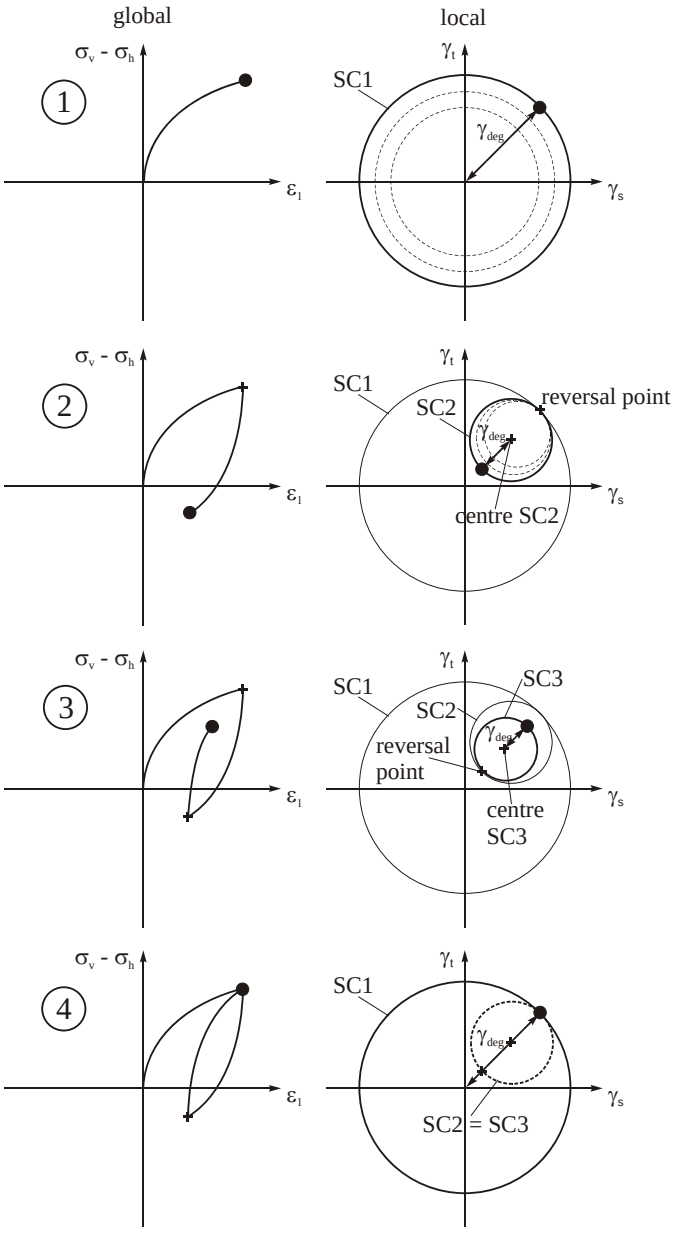

Figure 4. Schematic representation of global stress-strain curves and development of local shear strain contours in triaxial loading - unloading - reloading

1. Monotonic loading: Only 1 strain contour (SC) exists, whose centre is fixed at the origin of axis.
2. First load reversal: A second shear strain contour is created, which is fixed at the reversal point and gradually enlarged.
3. Second load reversal: A third strain contour is created, following the same procedure as in 2.
4. Intersection with primary loading path: The current load step enlarges the outer strain contour SC 1, hence all inner contours are erased and γ_{deg} is calculated from SC 1.

With that approach the two original and the two extended Masing rules (Pyke 1979) are fulfilled for the elastic part of the model:

1. For primary loading the stress-strain curve follows the back-bone curve.
2. After load reversal the size of the hysteretic loop is increased by a factor of 2.
3. If the past maximum shear strain is exceeded the stress-strain curve follows the backbone curve.
4. If an unloading-reloading curve intersects a previous unloading-reloading curve, it follows the previous curve.

The third Masing rule is treated as a special case of the fourth rule, as the primary strain contour differs from the others only by its fixed centre at the origin of axis. Rule 2 is fulfilled without modifying degradation parameters in unloading / reloading, as the shear strain controlling stiffness degradation refers to the centre of the strain contour rather than the reversal point.

In principle, an infinite number of strain contours could be taken into account. As the information of the local strain contours has to be stored as state variables, a limited number of four strain contours is considered in the model. It should be noted that still an infinite number of load cycles can be modeled, as only the number of load reversals going inside the primary strain contour is limited.

5. FIRST MODEL VALIDATION

5.1 Triaxial load cycles

Triaxial test simulation on isotropic elastic material demonstrate the capability of the strain contour approach to reproduce the Masing rules (Figure 5). The simulation starts at an isotropic compression stress state und involves various unloading – reloading loops. In particular, after a small unloading – reloading loop the stress – strain curve joins the previous curve once the previous strain level is exceeded, indicating fulfillment of the third Masing rule.

If the strain contour approach is coupled with an elastoplastic strain hardening model, no closed loops are obtained anymore if primary loading is involved (Figure 6). While the first, third and fourth Masing rule are still enforced, plastic strains result in faster stiffness degradation in primary loading than in unloading / reloading. Once the position of the yield surface is shifted during primary loading, the material behavior inside the yield surface is elastic (albeit with strain dependent stiffness). Plastic strains only occur if the previous stress level is exceeded.

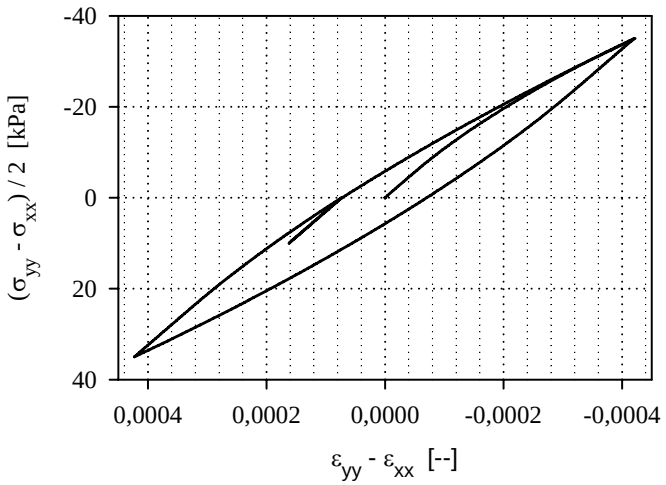

Figure 5. Triaxial loading / unloading / reloading loop for the elastic model

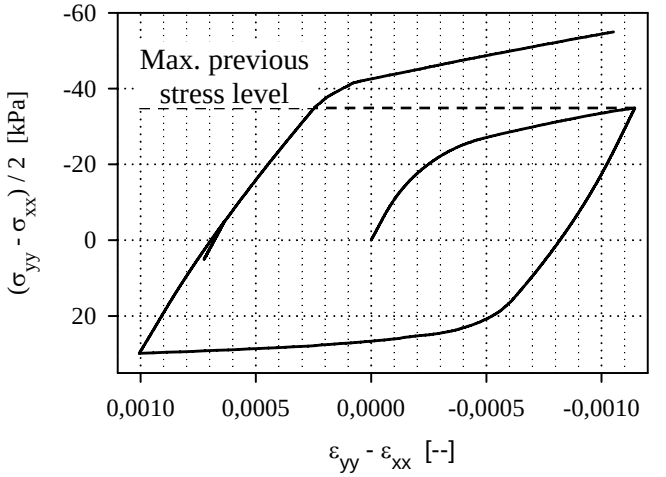

Figure 6. Triaxial loading / unloading / reloading loops for the elastoplastic strain hardening model

5.2 Biaxial tests

Starting at an initial stress state of $\sigma_{xx} = \sigma_{yy} = -100$kPa and $\sigma_{zz} = -40$kPa, biaxial strain increments $\varepsilon_{xx} = \varepsilon_{yy}$ and $\varepsilon_{zz} = 0$ are applied to an intrinsically isotropic material. At axial strain levels of 0.1%, 0.2% and 0.3% small strain steps are applied which enclose the angle α with the direction of the monotonic strain path (Figure 7). Degradation of small strain stiffness already takes place along the initial strain path. As shear strains evolve at different pace on different planes, the initially isotropic material becomes anisotropic during biaxial loading. In order to quantify the regain of shear stiffness with deviation from the monotonic strain path the tangent shear modulus has been derived from the increments of the second deviatoric stress and strain invariants J and E_d.

$$G_{\tan} = \Delta J / \Delta E_d \tag{18}$$

$$J = \frac{1}{\sqrt{6}}\sqrt{(\sigma_1-\sigma_2)^2+(\sigma_1-\sigma_3)^2+(\sigma_2-\sigma_3)^2} \tag{19}$$

$$E_d = \frac{2}{\sqrt{6}}\sqrt{(\varepsilon_1-\varepsilon_2)^2+(\varepsilon_1-\varepsilon_3)^2+(\varepsilon_2-\varepsilon_3)^2} \tag{20}$$

Figure 8 shows the small strain stiffness recovery in dependency on the deviation from the monotonic loading path. The shear stiffness obtained for the different strain increments only depends on the direction of the strain step, not on the strain level. At 0.1% axial strain slightly higher values of G_{tan} are observed, as not all relevant planes have reached the large strain range yet. From $\alpha = 0°$ to $\alpha = 140°$ the tangential stiffness increases gradually, as more and more local shear strain paths turn inside the primary strain contour. A minor increase in shear stiffness is already noticeable for $\alpha = 45°$, even though on local level the model enforces a change in stiffness only if the local shear strain increment deviates by more than 90° from the monotonic strain path. Beyond $\alpha = 140°$ the full initial shear stiffness is restored.

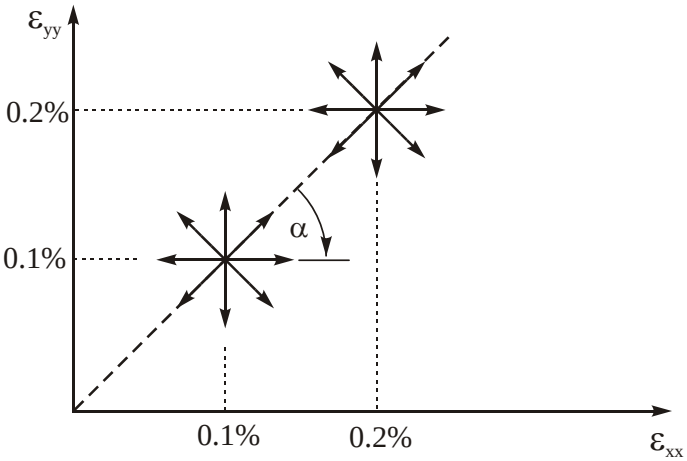

Figure 7. Simulated small strain steps in drained biaxial tests at different strain levels

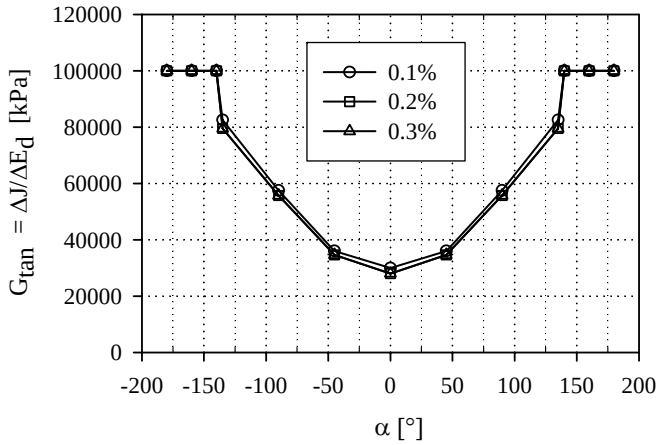

Figure 8. Elastic shear stiffness with varying deviation from monotonic loading

6. TRIAXIAL TESTS ON HAM RIVER SAND

6.1 Test results

Kuwano and Jardine (2002) conducted numerous bender element aided triaxial tests on loose and dense Ham River Sand (HRS) in order to investigate the applicability of cross anisotropic elasticity at very small strains. Their findings can be summarized as follows:

1. The concept of cross anisotropic elasticity describes soil behavior within the small strain region reasonably well.
2. Axial Young's and shear moduli vary strongly with effective stress level. Empirical correlations are proposed with E_h and E_v depending on the corresponding axial stresses σ_h and σ_v, while the shear moduli G_{hh} and G_{vh} depend on a combination of the axial stresses (eq. 21). Beyond a stress ratio $R = \sigma_h / \sigma_v$, > 2.2 these relationships are not applicable any more due to dilation.
3. Unloading – reloading loops at unloading stress states show evidence of kinematic yielding.

$$E_h = f(e)\cdot C_h \cdot \left(\frac{\sigma_h}{p_{ref}}\right)^{b_h} \;;\; E_v = f(e)\cdot C_v \cdot \left(\frac{\sigma_v}{p_{ref}}\right)^{a_v}$$

$$G_{vh} = f(e)\cdot C_{vh} \cdot \left(\frac{\sigma_v}{p_{ref}}\right)^{a_{vh}} \cdot \left(\frac{\sigma_h}{p_{ref}}\right)^{b_{vh}} \tag{21}$$

$$G_{hh} = f(e)\cdot C_{hh} \cdot \left(\frac{\sigma_v}{p_{ref}}\right)^{a_{hh}} \cdot \left(\frac{\sigma_h}{p_{ref}}\right)^{b_{hh}}$$

Table 1. Anisotropic small strain stiffness moduli for Ham River Sand (Kuwano and Jardine 2002)

	E_v	E_v	G_{vh}	G_{hh}
C [MPa]	204	174	72	81
a	0.52	--	0.32	-0.04
b	--	0.53	0.20	0.53

The function $f(e) = (2.17 - e)^2 / (1+e)$ accounts for variability of elastic stiffness with void ratio e. Poisson's ratios cover a range of $\nu_{vh} = 0.2 \ldots 0.4$ and $\nu_{hh} = 0.05 \ldots 0.2$.

6.2 Stress dependency

The two approaches presented in section 3.3 are compared with the experimental data for the cross anisotropic stress state ($K_0 = 0.45$) in Figure 9. Constant values of $_{vh} = 0.3$, $\nu_{hh} = 0.07$ and $f(e) = 1.37$ are applied. While G_{vh} and G_{hh} (not shown) match the experimental data reasonably well, distinct differences can be observed for the axial moduli. Both approaches deliver higher values for E_h and lower values for E_v than observed experimentally. Even though in approach 2 local stiffness moduli depend on the normal stress on that plane (which is the same as the axial stresses for orientations perpendicular to these axes), due to the

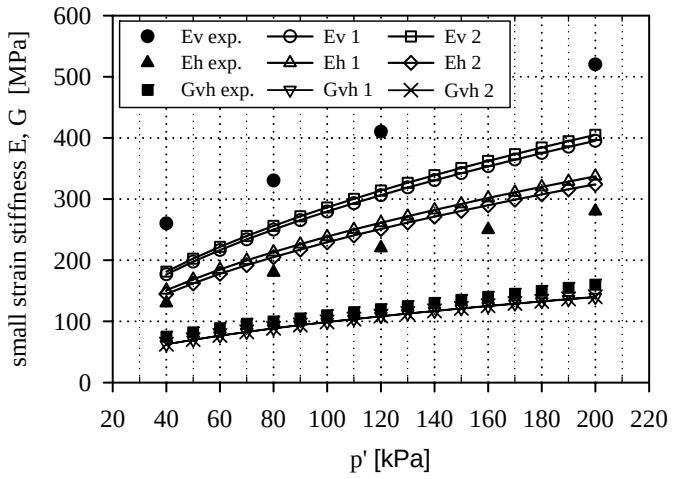

Figure 9. Stiffness moduli with varying mean effective stress at an anisotropic stress state (K_0 = 0.45, e = 0.66)

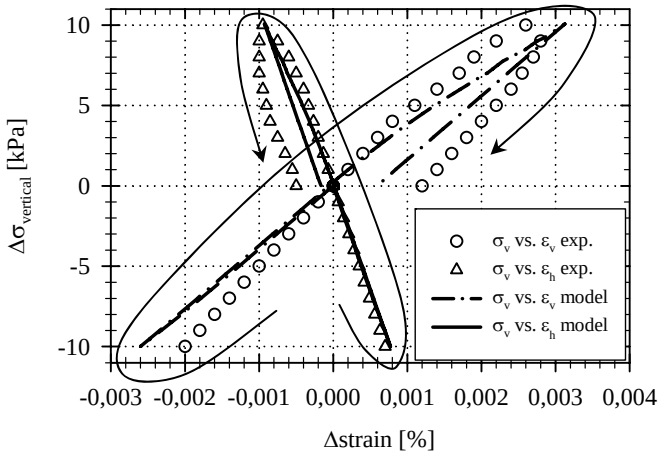

Figure 10. Stress – strain curves for vertical unloading–reloading loops at an anisotropic initial stress state (σ_v = 316kPa, σ_h = 142kPa, e = 0.66)

summation of the contributions of all planes the difference between both approaches on global level is negligible.

The considerable difference between the modeled stress dependency and the experimental data raises the question why the elastic part of the model was not implemented according to eq. 21. In fact it turned out that such stress dependency has consequences if used as the elastic part of an elasto-plastic constitutive model. Even for an isotropic material with $E_{h,ref} = E_{v,ref}$, material behavior will be anisotropic for any non-isotropic stress state. For a smooth transition from small-strain (purely elastic) to large strain (elasto-plastic) behavior the stress dependency of elastic stiffness moduli must be the same in both strain regions. Hence, also the calculation of plastic strains had to be based on an anisotropic hyperelastic part. For macroscopic plasticity such a model is proposed by Gajo (2009). However, incorporating anisotropic elasticity in the calculation of plastic strains in multilaminate models is beyond the scope of this study.

6.3 Stress / strain paths

The drained triaxial test starts at an nearly K_0 – anisotropic stress state. It is reported that the material was allowed to age before testing, which is taken into account in the simulation by deleting all traces of strain history in the material (resetting of state variables concerning strain contours). At first the vertical stress is reduced by 10kPa (unloading). Then the specimen is reloaded beyond the stress state at the start of the test by a margin of 10kPa. Finally the vertical stress is again reduced by 10kPa to get back to the initial stress state. The horizontal stress σ_h was held constant during the test.

Simulation results (Figure 10) show that the modeled behavior at load reversals in general matches well with the experimental results. The inclination of the predicted $\sigma_v - \varepsilon_v$ curve is slightly lower due to the lower vertical stiffness E_v discussed in section 6.2. The difference in the curves for positive and negative $\Delta\sigma_v$ are caused by the occurrence of plastic strains once the previous stress level is exceeded, which results in faster degradation of stiffness in primary loading than in unloading/reloading.

In the experiment further unloading-reloading loops were carried out at different stress states, which are not considered here. However, it should be noted that these tests showed evidence of kinematic hardening, which can not be taken into account by the elastoplastic model used in this study. Capturing such behavior would be essential in modeling repeated cyclic loading as in earthquakes or other types of dynamic loading. The model presented in this study is therefore restricted to cases in which only a limited number of unloading–reloading cycles take place, which usually is sufficient for typical geotechnical engineering problems.

7. CONCLUSIONS

A novel approach to modeling cross anisotropic small strain stiffness and behavior at load reversals within the multilaminate framework has been presented. The anisotropic elastic small strain part is coupled with an isotropic strain hardening plasticity model at intermediate and larger strains. Anisotropy in stiffness is assumed to diminish with accumulating shear strain. Load reversals are detected by memorizing local shear strain paths.

The proposed model obeys all four Masing rules and matches well with soil behavior at load reversal observed in experiments. However, the modeled dependency of stiffness moduli on mean effective stress p’ or on plane normal stress does not fully match with experimental results, where axial moduli were found to depend on the corresponding axial stresses. In numerical simulations of boundary value problems this discrepancy can be approximately accounted for by choosing input moduli according to the initial anisotropic stress state.

REFERENCES

Bažant, Z.P. and Oh, B.H. (1986). "Efficient Numerical Integration on the Surface of a Sphere," Zeitschrift für angewandte Mathematik und Mechanik 66, 37-49

Bažant, Z.P. and Prat, P.C. (1988). "Microplane Model for Brittle-Plastic Material: I. Theory," Journal of Engineering Mechanics 114(10), 1672-1688

Benz, T., Vermeer, P.A. and Schwab, R. (2009). "A small-strain overlay model," International Journal for Numerical and Analytical Methods in Geomechanics 33(1), 25-44

Fioravante, F. (2000). "Anisotropy of small strain stiffness of Ticino and Kenya sands from seismic wave propagation measured in triaxial testing," Soils and Foundations 40(4), 129-142

Gajo, A. (2009) "Hyperelastic modelling of small-strain stiffness anisotropy of cyclically loaded sand," International Journal for Numerical and Analytical Methods in Geomechanics 34(2), 111-134

Gasparre, A. (2005). Advanced laboratory characterisation of London Clay. PhD thesis, Imperial College, London

Kuwano, R. and Jardine, R.J. (2002). "On the applicability of cross-anisotropic elasticity to granular materials at very small strains," Geotechnique 52(10), 727-749

Pyke, R.M. (1979). "Nonlinear soil models for irregular cyclic loadings," Journal of the Geotechnical Engineering Division, ASCE, 105(GT6), 715-726

Schädlich, B. and Schweiger, H.F. (2010). "Modelling anisotropic small strain stiffness within the multilaminate framework," Proc. of the 7th European Conference on Numerical Methods in Geotechnical Engineering, Benz & Nordal, eds., Taylor & Francis Group, London, 679-684

Schweiger, H.F., Wiltafsky, C., Scharinger, F. and Galavi, V. (2009). „A multilaminate framework for modelling induced and inherent anisotropy of soils," Geotechnique 59(2), 87-101

Schweiger, H.F. and Schädlich, B. (2011). "Influence of modelling soil anisotropy on the behaviour of deep excavations," Proc. of the 13th Intern. Conference of the International Association for Computer Methods and Advances in Geomechanics, in press

Simpson, B. (1992) "Retaining structures - displacement and design," Geotechnique 42(4), 539-576

APPENDIX

Macroscopic cross anisotropic compliance matrix (in Kelvin notation):

$$\mathbf{C}_{gl,Kelvin} = \begin{pmatrix} \frac{1}{E_h} & \frac{-\nu_{hv}}{E_h} & \frac{-\nu_{hh}}{E_h} & 0 & 0 & 0 \\ \frac{-\nu_{hv}}{E_h} & \frac{1}{E_v} & \frac{-\nu_{hv}}{E_h} & 0 & 0 & 0 \\ \frac{-\nu_{hh}}{E_h} & \frac{-\nu_{hv}}{E_h} & \frac{1}{E_h} & 0 & 0 & 0 \\ 0 & 0 & 0 & \frac{1}{2G_{vh}} & 0 & 0 \\ 0 & 0 & 0 & 0 & \frac{1}{2G_{vh}} & 0 \\ 0 & 0 & 0 & 0 & 0 & \frac{1+\nu_{hh}}{E_h} \end{pmatrix} \quad \text{(A.1)}$$

Eigenvalues of cross anisotropic compliance matrix:

$$\lambda_1 = \frac{\nu_{hh}+1}{E_h}. \quad \text{(A.2a)}$$

$$\lambda_2 = \frac{1-\nu_{hh}}{2E_h} + \frac{1}{2E_v} - \sqrt{\left(\frac{1-\nu_{hh}}{2E_h} - \frac{1}{2E_v}\right)^2 + \frac{2{\nu_{hv}}^2}{{E_h}^2}} \quad \text{(A.2b)}$$

$$\lambda_3 = \frac{1-\nu_{hh}}{2E_h} + \frac{1}{2E_v} + \sqrt{\left(\frac{1-\nu_{hh}}{2E_h} - \frac{1}{2E_v}\right)^2 + \frac{2{\nu_{hv}}^2}{{E_h}^2}} \quad \text{(A.2c)}$$

$$\lambda_4 = \frac{1}{2G_{vh}} \quad \text{(A.2d)}$$

Eigenangle:

$$\tan 2\omega = \frac{-2\cdot\sqrt{2}\cdot\frac{\nu_{hv}}{E_v}}{\frac{1-\nu_{hh}}{E_h}+\frac{1}{E_v}} \quad \text{(A.3)}$$

Idempotent matrices for cross anisotropic material:

$$\mathbf{E}_1 = \begin{pmatrix} 1/2 & 0 & -1/2 & 0 & 0 & 0 \\ 0 & 0 & 0 & 0 & 0 & 0 \\ -1/2 & 0 & 1/2 & 0 & 0 & 0 \\ 0 & 0 & 0 & 0 & 0 & 0 \\ 0 & 0 & 0 & 0 & 0 & 0 \\ 0 & 0 & 0 & 0 & 0 & 1 \end{pmatrix} \quad \text{(A.4a)}$$

$$\mathbf{E}_2 = \begin{pmatrix} \frac{\cos^2\varpi}{2} & \frac{\cos\varpi\sin\varpi}{\sqrt{2}} & \frac{\cos^2\varpi}{2} & 0 & 0 & 0 \\ \frac{\cos\varpi\sin\varpi}{\sqrt{2}} & \sin^2\varpi & \frac{\cos\varpi\sin\varpi}{\sqrt{2}} & 0 & 0 & 0 \\ \frac{\cos^2\varpi}{2} & \frac{\cos\varpi\sin\varpi}{\sqrt{2}} & \frac{\cos^2\varpi}{2} & 0 & 0 & 0 \\ 0 & 0 & 0 & 0 & 0 & 0 \\ 0 & 0 & 0 & 0 & 0 & 0 \\ 0 & 0 & 0 & 0 & 0 & 0 \end{pmatrix} \quad \text{(A.4b)}$$

$$\mathbf{E}_3 = \begin{pmatrix} \frac{\sin^2\varpi}{2} & \frac{\cos\varpi\sin\varpi}{-\sqrt{2}} & \frac{\sin^2\varpi}{2} & 0 & 0 & 0 \\ \frac{\cos\varpi\sin\varpi}{-\sqrt{2}} & \cos^2\varpi & \frac{\cos\varpi\sin\varpi}{-\sqrt{2}} & 0 & 0 & 0 \\ \frac{\sin^2\varpi}{2} & \frac{\cos\varpi\sin\varpi}{-\sqrt{2}} & \frac{\sin^2\varpi}{2} & 0 & 0 & 0 \\ 0 & 0 & 0 & 0 & 0 & 0 \\ 0 & 0 & 0 & 0 & 0 & 0 \\ 0 & 0 & 0 & 0 & 0 & 0 \end{pmatrix} \quad \text{(A.4c)}$$

$$\mathbf{E}_4 = \begin{pmatrix} 0 & 0 & 0 & 0 & 0 & 0 \\ 0 & 0 & 0 & 0 & 0 & 0 \\ 0 & 0 & 0 & 0 & 0 & 0 \\ 0 & 0 & 0 & 1 & 0 & 0 \\ 0 & 0 & 0 & 0 & 1 & 0 \\ 0 & 0 & 0 & 0 & 0 & 0 \end{pmatrix} \quad \text{(A.4d)}$$